

# Paying more attention to local contrast: improving infrared small target detection performance via prior knowledge

Peichao Wang, Jiabao Wang, Yao Chen, Rui Zhang\*, Yang Li and Zhuang Miao

Command and Control Engineering College, Army Engineering University of PLA, Nanjing, 210017, Jiangsu, China

## ARTICLE INFO

### Keywords:

Infrared image  
Small target detection  
Prior knowledge  
Local contrast  
Channel attention  
Lightweight

## ABSTRACT


The data-driven method for infrared small target detection (IRSTD) has achieved promising results. However, due to the small scale of infrared small target datasets and the limited number of pixels occupied by the targets themselves, it is a challenging task for deep learning methods to directly learn from these samples. Utilizing human expert knowledge to assist deep learning methods in better learning is worthy of exploration. To effectively guide the model to focus on targets' spatial features, this paper proposes the Local Contrast Attention Enhanced infrared small target detection Network (LCAE-Net), combining prior knowledge with data-driven deep learning methods. LCAE-Net is a U-shaped neural network model which consists of two developed modules: a Local Contrast Enhancement (LCE) module and a Channel Attention Enhancement (CAE) module. The LCE module takes advantages of prior knowledge, leveraging handcrafted convolution operator to acquire Local Contrast Attention (LCA), which could realize background suppression while enhance the potential target region, thus guiding the neural network to pay more attention to potential infrared small targets' location information. To effectively utilize the response information throughout downsampling progresses, the CAE module is proposed to achieve the information fusion among feature maps' different channels. Experimental results indicate that our LCAE-Net outperforms existing state-of-the-art methods on the three public datasets NUDT-SIRST, NUAA-SIRST, and IRSTD-1K, and its detection speed could reach up to 70 fps. Meanwhile, our model has a parameter count and Floating-Point Operations (FLOPs) of 1.945M and 4.862G respectively, which is suitable for deployment on edge devices.

## 1. Introduction

Visible light imaging is easily disrupted by external environmental factors and can be difficult to operate effectively in complex environments. Comparing to it, infrared imaging has obvious advantages in anti-interference (Luo et al., 2010). Additionally, infrared imaging can operate at long distances in all-weather, making it widely used in fields such as early warning and space-based surveillance systems (Hu et al., 2024). Compared to radar, infrared detection equipment does not need to actively emit detection signals and possess strong concealment, thus playing a significant role in complex battlefield environments. Effectively detecting of the infrared small targets has always been an important and challenging task in this field. According to the Society of Photo-Optical Instrumentation Engineers (SPIE), typical infrared small targets have characteristics such as contrast ratio less than 15%, Signal-to-Noise Ratio (SNR) less than 1.5, and target size less than 0.15% of the entire image (Chapple et al., 1999).

To effectively detect infrared small targets, researchers have proposed a large number of methods. Existing methods can be broadly divided into two categories: model-driven methods and data-driven methods (Kou et al., 2023). Model-driven methods primarily involve handcrafted models and do not require the support of large amounts of data. These methods usually follow specific assumptions, with the aim of purely using experts' prior knowledge to find out the targets, such as looking for outliers with discontinuous grayscale in slowly transitioning backgrounds (Wang et al., 2024). Model-driven methods are significantly impacted by backgrounds and noise, exhibiting heightened sensitivity to hyperparameters such as pre-defined window sizes and segmentation thresholds. This necessitates iterative fine-tuning and experimentation tailored to specific scenarios, ultimately compromising their robustness and adaptability. Data-driven methods mainly rely on deep learning models, leveraging supervised learning techniques to empower the deep neural networks with the capability to autonomously learn features from diverse datasets, demonstrating robust generalization across varied scenes. With the rapid advancements of deep learning technologies, infrared small target

\*Corresponding author

 rzhang\_aeu@163.com (R. Zhang)

detection (IRSTD) methods based on Convolutional Neural Networks (CNN) (Sun et al., 2023; Zhang et al., 2023; Chen et al., 2022) and transformer architectures (Yuan et al., 2024; Wang et al., 2022; Yang et al., 2024) have been proposed, which have achieved good detection results. However, the challenges associated with acquiring high-quality infrared images and annotations significantly constrain purely data-driven methods. Additionally, CNN and transformer-based networks typically encompass a vast number of parameters, posing difficulties in their deployment on edge devices with limited computational capabilities.

In recent years, hybrid detection methods that combine model-driven and data-driven approaches have brought new possibilities. By seamlessly integrating prior knowledge inherent in model-driven methods into deep learning frameworks, these hybrid methods have witnessed improvements in terms of model performance, parameter size and computational complexity. Researchers have proposed hybrid detection models including RDIAN (Receptive-Field and Direction Induced Attention Network) (Sun et al., 2023), ALCNet (Attentional Local Contrast Network) (Dai et al., 2021b) and MSDA-Net (Multi-Scale Direction-Aware Network) (Zhao et al., 2024), and so on. These methods mainly insight from human visual system (HVS) and create multiscale dilated convolution operators to emphasis one pixel's local contrast. However, different scale may pose different effects on detection performance, it is wise to figure out the influence of one operator instead of directly adding or concatenating multiscale operators to create new feature maps. Based on this intuition, we propose the Local Contrast Enhancement (LCE) module. In this module, we compute the Local Contrast Attention (LCA) as an indicator to emphasize potential targets while suppressing the background surrounding them, guiding neural networks to precisely pinpoint potential locations of infrared small targets. Furthermore, to facilitate efficient cross-channel information fusion and maintain semantic information of small targets during downsampling stages, we present the Channel Attention Enhancement (CAE) module. Combining these two innovative modules, we propose the Local Contrast Attention Enhanced infrared small target detection Network (LCAE-Net). This model has advantages in parameter size and Floating-Point Operations (FLOPs) compared to current detection methods and has achieved excellent test results on the three benchmark datasets—NUAA-SIRST, NUDT-SIRST, and IRSTD-1K, effectively striking a balance between performance and computational efficiency.

In summary, our contributions are summarized below:

- LCAE-Net is proposed as the integration of model-driven and data-driven method, which introduces prior knowledge to sufficiently utilize local contrast information. It is an effective U-shaped neural network model that fully utilizes prior knowledge to boost the model performance.
- A LCE module which leverages prior knowledge to enhance the local contrast features of potential infrared small targets is proposed, effectively guiding the constructed neural network model to capture the location information of potential targets.
- A CAE module is proposed, achieving fusion of information among different channels in the multi-scale feature maps obtained from downsampling.
- Experiments on three public benchmark datasets demonstrated remarkable performance of our method. Comparing to several state-of-the-art detection methods, LCAE-Net has successfully achieved a balance between superior performance and efficient computation, indicating its potential effectiveness on edge devices.

## 2. Related works

### 2.1. Model-driven infrared small target detection methods

In early stages, IRSTD tasks mainly relied on traditional model-based methods, which can be further divided into background suppression-based methods, optimization-based methods, and HVS-based methods. Background suppression-based methods (Deshpande et al., 1999; Zeng et al., 2006; Cui et al., 2024) regard infrared small targets as outliers in the original image and obtain target information through filtering algorithms, while optimization-based methods (Gao et al., 2013; Dai et al., 2016; Wu et al., 2024) consider infrared small targets have sparse characteristics in images which could be separated from background pixels through matrix decomposition. Comparing these two kinds of methods, HVS-based methods have more physical meanings.

Contrast is the most important quantity in the visual system's flow coding (Chen et al., 2013), and the human visual system can be quickly attracted to small targets on infrared images (Zhao et al., 2022). Inspired by this, methods based on HVS learn from selective mechanism of the human eye's rapid response to visually salient regions, using

local contrast to achieve the detection of infrared small targets. Chen et al. (2013) proposed the classic Local Contrast Measure (LCM) method, which uses local contrast features to highlight the target and employs adaptive thresholding for target extraction. Wei et al. (2016) improved the LCM's limitation to bright targets and proposed the MPCM (Multiscale Patch-based Contrast Measure) method, which enhances both bright and dark targets and uses parallel computing to improve real-time performance. Xia et al. (2019) further proposed the Local Energy Factor (LEF) based on LCM, an indicator for measuring the dissimilarity between the target area and the surrounding background, enriching the description of local image differences, and achieving target segmentation and extraction through adaptive thresholding when combined with LCM. He et al. (2024) proposed the variance difference weighted three-layer local contrast measure (VDWTLCM) method to effectively suppress highlight backgrounds and strong noise, where the three-layer local contrast measure (TLCM) module calculates the local contrast of a single pixel for target enhancement and background suppression, and the weighting function based on the mean value of the variance difference (MVD) further suppresses prominent background edges. Zhang et al. (2024) used density peak search to find candidate target positions in images preprocessed with Gaussian differentiation, enhanced the gradient saliency features of candidate targets using local contrast methods for background suppression, and determined the target position through threshold segmentation after calculating and fusing multi-directional gradient features. Contrast-based algorithms are designed by referencing the principles of how the human visual system observes objects and have relatively strong interpretability, providing the possibility of integrating prior knowledge into deep learning models.

## 2.2. Data-driven infrared small target detection methods

Due to the limited number of pixels occupied by infrared small targets in images, directly applying typical object detection methods such as R-CNN (Girshick et al., 2014), YOLO (Redmon et al., 2016), and SSD (Liu et al., 2016) to IRSTD field often leads to poor performance. As a result, researchers usually model it as a pixel-level binary classification problem (Wang et al., 2019).

IRSTD methods based on CNN are currently prevalent in research. Dai et al. (2021a) introduced the Asymmetric Contextual Modulation (ACM) module, which effectively realized the fusion of shallow and deep features, with its efficacy validated through experiments on Feature Pyramid Network (FPN) and U-Net. Li et al. (2022) relieved the issue of response vanishing due to deeper network layers by proposing the DNA-Net (Dense Nested Attention Network), which repeatedly fuses and enhances multi-level features through dense connections, fully integrating and utilizing the contextual information of small targets. Hou et al. (2022) proposed the ISTDU-Net (Infrared Small-Target Detection U-Net), which improves the downsampling and skip connections of traditional U-Net by introducing feature map groups and fully connected layers to enhance small target weights and increase the global receptive field. Zhang et al. (2022b) proposed the ISNet (Infrared Shape Network), exploring the use of the Taylor Finite Difference (TFD) module for edge detection and the Two-Orientation Attention Aggregation (TOAA) module for the fusion of low-level and high-level information in both row and column directions, capturing target shape features and suppressing noise. Wu et al. (2022) developed the UIU-Net (U-Net in U-Net), embedding a small U-Net within a large U-Net backbone network to achieve multi-level and multi-scale representation learning of targets while mitigating the issue of deep response vanishing for small targets. Liu et al. (2024) pointed out that while much research focuses on the design of the network itself, there is insufficient exploration of the loss function area, thus they proposed a new Scale and Location Sensitive (SLS) loss to assist U-shaped networks in distinguishing and locating targets of different scales, and further developed the MSHNet (Multi-Scale Head to the plain U-Net) based on this loss function. With the introduction of Vision Transformer (ViT), the application of Transformer models in IRSTD tasks (Liu et al., 2023a; Wu et al., 2023; Yuan et al., 2024) has become increasingly common. Additionally, methods based on diffusion models (Shi et al., 2024), graph neural networks (Jia et al., 2024) and state space models (Tianxiang et al., 2024) have also been proposed. Purely data-driven methods often resort to complex connections among different layers to preserve small targets' responses, and promote model performance at the cost of increased parameters and computational costs.

## 2.3. Hybrid infrared small target detection methods

Improving model performance at the cost of increasing model complexity is not a long-term solution. Since model-driven methods effectively utilize the expertise of human experts, combining them with deep learning methods can effectively integrate prior knowledge into deep learning models, thereby enhancing the detection performance of proposed models.

Insights in HVS are popular in this field. Dai et al. (2021b) drew inspiration from DeepLab series (Yu and Koltun, 2015) and MPCM (Wei et al., 2016), embedding traditional multi-scale local contrast method into the end-to-end

network model ALCNet as a parameter-free linear layer, which realized a integration of model-driven and data-driven approaches. Yu et al. (2022) proposed a Multiscale Local Contrast Learning Network (MLCL-Net) that integrates local contrast into network training to generate local contrast feature maps. Sun et al. (2023) considered that a small target usually appears as a bright spot area with a Gaussian-like distribution, and grayscale differences between the central and boundary pixels exist in all the directions, which is known as multidirectionality. Inspired by this prior knowledge, they proposed RDIAN, which consists of one Multi-Directional Target Enhancement (MDTE) module aiming at enhancing target features in low-level feature maps. Nian et al. (2023) changed the approach of acquiring local contrast and developed multiple attention local contrast module stemmed from ALCNet, then integrated it into their developed Local Contrast Attention Guide Network (LCAGNet) to promote detection performance. Zhao et al. (2024) utilized the prior knowledge of targets and constructed Multi-Directional Feature Awareness (MDFA) module to emphasize the focus on high-frequency directional features. However, due to the small area occupied by infrared small targets in the image, applying multiscale convolution operators to obtain feature maps at different scales may not necessary; in fact, even with single-scale convolution operator, we can achieve good results with lower computational complexity guided by prior knowledge.

### 3. Proposed method

#### 3.1. Overall pipeline

Fig. 1 illustrates the main framework of LCAE-Net proposed in this paper. The framework comprises three primary stages: an encoding stage, an enhancing stage, and a decoding stage.

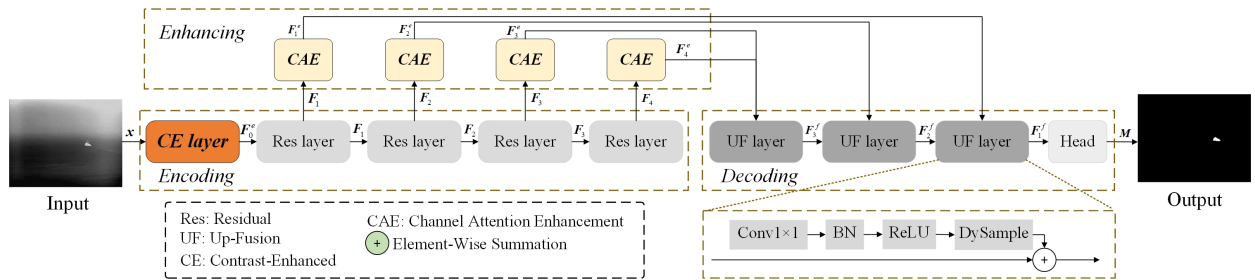


Fig. 1: Overview of the proposed LCAE-Net.

Given an infrared grayscale image  $x \in \mathbf{R}^{1 \times H \times W}$ , where  $H$  and  $W$  denote the height and width of the image. LCAE-Net initially employs the encoding stage to perform channel expansion and acquire multi-scale feature maps. The residual layer expands the channels of the input feature map  $F_0^e$  and performs spatial downsampling, thereby extracting a multi-scale feature map that contains contextual semantic information. Each layer consists of different numbers of ResNeSt blocks, denoted by  $N_i (i = 1, 2, 3, 4)$  which represents the number of blocks in each layer. For the input feature map  $F_0^e$ , after being processed through each layer, the resulting feature map  $F_i \in \mathbf{R}^{C_i \times H_i \times W_i}$  is obtained, where  $C_i$ ,  $H_i$  and  $W_i$  represent the number of channels, height, and width of the obtained feature map respectively. The ResNeSt block is the main building block of the ResNeSt network (Zhang et al., 2022a), which draws inspiration from SENet (Hu et al., 2020) and ResNeXt (Li et al., 2019). It introduces the concept of a cardinal group, where each group uses split-attention (SA) to obtain weights between channels, enhancing the interaction between different channels of information and improving the performance of downstream tasks. In our paper, we learn from the design concept of ISTDU-Net and sets  $N_i$  to 1, 2, 4, and 8. Through the implementation of SA, the correlation between channels of the input feature map is effectively enhanced, thereby improving the ability of cross-channel information interaction. This enables the model to better achieve the extraction of high-quality feature maps.

Subsequently, the enhancing stage effectively integrates and enhances information among different channels of four residual layers' output feature maps, preventing feature degradation from direct summation, and forwards the enhanced feature maps to the decoding stage.

The decoding stage comprises three up-fusion layers and one prediction head. The up-fusion layer performs upsampling on the input low-level feature map, reducing the number of channels while increasing the spatial resolution. The low-level feature map  $F_4^e$ ,  $F_3^f$  and  $F_2^f$  with an input size of  $2C \times H/2 \times W/2$  undergoes a dimension reduction operation through a  $1 \times 1$  convolution, reducing the dimension of the input feature map from  $2C$  to  $C$ . Then the

channel-reduced feature map is processed by a batch normalization layer and activated by ReLU function. We utilize the DySample (Liu et al., 2023b) lightweight dynamic upsampling operator on it to output a feature map of size  $C \times H \times W$  that aligns with the feature map  $F_i^e (i = 1, 2, 3)$  of the same level. Subsequently, the two aligned feature maps are added together to realize feature fusion and reconstruction, outputting the fused feature map  $F_i^f$ . After employing three consecutive feature fusion and reconstruction operations, the resulting feature map  $F_1^f$  is sent into the prediction head to generate point-by-point prediction results for each pixel. The prediction head processes the feature map  $F_1^f$  with  $3 \times 3$  convolution, batch normalization layer, ReLU activation function and  $1 \times 1$  convolution sequentially, and activates the output through the sigmoid function, thus a probability feature map  $M' \in \mathbf{R}^{1 \times H \times W}$  is generated. Each value on this feature map represents the probability of the corresponding pixel belonging to the target. Here, the value of the pixels with a probability greater than 0.5 is set to 1 while the rest are set to 0, resulting in a prediction mask  $M \in \mathbf{R}^{1 \times H \times W}$  which is consistent in size with the original input image.

### 3.2. Local Contrast Enhancement module

The Local Contrast Enhancement (LCE) is the core module of the Contrast-Enhanced (CE) layer, which is the first layer of the proposed model. The CE layer processes the input infrared grayscale image, expanding its channels and enhancing extracted feature responses with the aid of LCE module. The LCE module is employed to derive attention weights for potential infrared small targets within the original image. These attention weights reflect probabilities whether current pixel is located in target areas. The LCE module's essence resides in fusing human expert knowledge into designing convolution operators. These operators integrate prior knowledge, effectively mitigating the blindness and tendency to fall into local extrema that often accompany with autonomous learning in deep neural networks. Specifically, as the first processing module, its optimization during training is highly susceptible to the influence of backpropagation gradients from subsequent modules. This can lead to issues such as slow parameter learning caused by gradient accumulation errors and a propensity to get stuck in local optima. By employing artificially designed convolution operators, we can effectively guide the neural network to focus on targets that we concern. The structures of the CE layer and LCE module are depicted in Fig. 2.

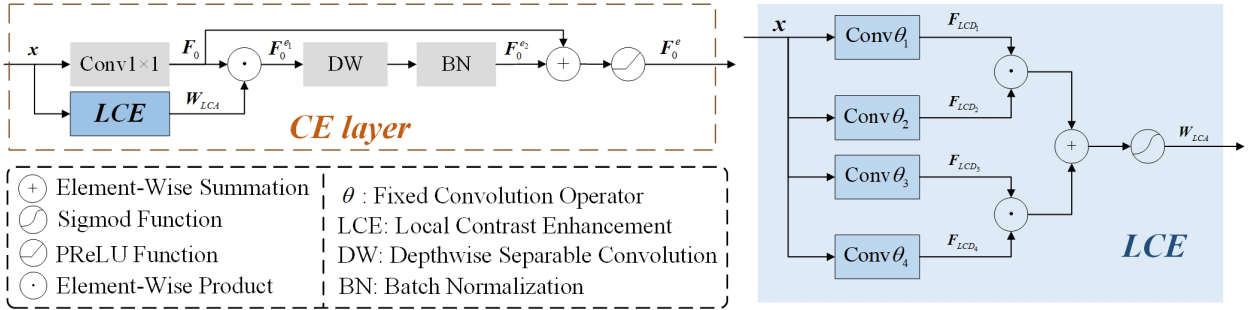


Fig. 2: Structures of the CE layer and LCE module.

Given an infrared grayscale image  $x \in \mathbf{R}^{1 \times H \times W}$ , it initially passes through a  $1 \times 1$  convolution kernel for channel expansion, yielding the primary feature map  $F_0 \in \mathbf{R}^{C \times H \times W}$ , where  $C$  denotes the number of channels after expansion. Simultaneously, the original image is processed by the LCE module to output the matrix (attention weights)  $W_{LCA} \in \mathbf{R}^{1 \times H \times W}$ . One infrared small target generally exhibits Gaussian-like distributions in images, and the gray value of small targets usually spreads uniformly in its surroundings (Sun et al., 2023). The gray value of an infrared small target is generally higher than surrounding background pixels, which means it has high local contrast. The visual attention mechanism is an important foundation for HVS, and human eyes will quickly focus on the important areas in the scene (M, 2011). Gaussian distribution typically features a bell-shaped curve, peaking in the middle and tapering off gradually towards the surrounding sides. Based on above prior knowledge, it is advisable for us to have a measure to present this local characteristic. Here, we propose the Local Contrast Distance (LCD) to precisely capture this local characteristic. For the input grayscale image  $x$ , we define the following operations to acquire feature map  $F_{LCD_i} (i = 1, 2, 3, 4)$  which contains local contrast information:

$$F_{LCD_i} = \theta_i \otimes x \quad (1)$$

where  $\otimes$  denotes convolution operation,  $\theta_i$  denotes the  $L \times L$  fixed convolution operator with dilation rate  $d$ , each value within  $F_{LCD_i}$  signifies the  $LCD$  value of each pixel in the original image computed by using a fixed convolution operator  $\theta_i$ . Here, we illustrate the structure of each fixed convolution operator by setting its center coordinate as  $(0, 0)$ , as depicted in Fig. 3.

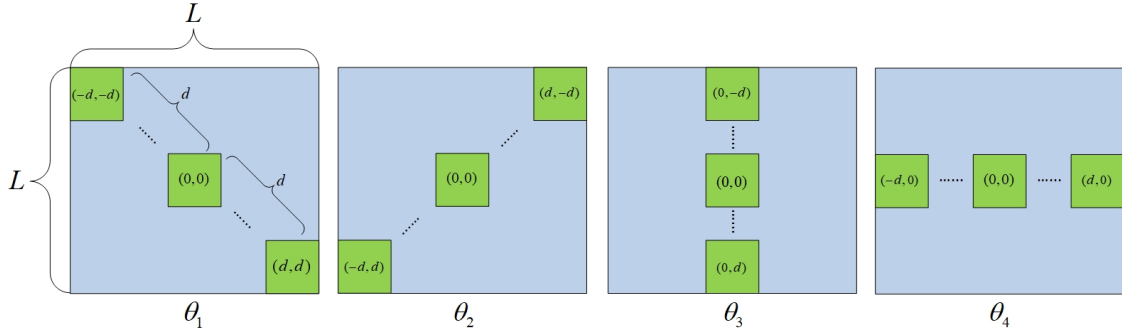


Fig. 3: Structures of our fixed convolution operators.

Each convolution operator, with the exception of green marked positions, comprises zeros in all other locations. Specifically, when applied to a pixel at coordinate  $(m, n)$  within the original image  $\mathbf{x}$ , four  $LCD$  values can be obtained through the following computations:

$$\begin{aligned}
 F_{LCD_1}(m, n) &= \theta_1(0, 0) \times \mathbf{x}(m, n) - \theta_1(-d, -d) \times \mathbf{x}(m-d, n-d) - \theta_1(d, d) \times \mathbf{x}(m+d, n+d) \\
 F_{LCD_2}(m, n) &= \theta_2(0, 0) \times \mathbf{x}(m, n) - \theta_2(-d, d) \times \mathbf{x}(m-d, n+d) - \theta_2(d, -d) \times \mathbf{x}(m+d, n-d) \\
 F_{LCD_3}(m, n) &= \theta_3(0, 0) \times \mathbf{x}(m, n) - \theta_3(0, -d) \times \mathbf{x}(m, n-d) - \theta_3(0, d) \times \mathbf{x}(m, n+d) \\
 F_{LCD_4}(m, n) &= \theta_4(0, 0) \times \mathbf{x}(m, n) - \theta_4(-d, 0) \times \mathbf{x}(m-d, n) - \theta_4(d, 0) \times \mathbf{x}(m+d, n)
 \end{aligned} \tag{2}$$

here  $\mathbf{x}(m, n)$  denotes the gray scale of the pixel situated at the coordinate  $(m, n)$  on the original image. Since infrared small targets exhibit a Gaussian-like distribution, where the central pixels within the target exhibit higher gray values while the boundary pixels possess relatively lower and comparable gray values, we set the central pixel value of fixed convolution operator as  $\alpha$  and other non-zero values as  $\beta$ , thus the above formulas could be simplified as follows:

$$\begin{aligned}
 F_{LCD_1}(m, n) &= \alpha \times \mathbf{x}(m, n) - \beta \times (\mathbf{x}(m-d, n-d) + \mathbf{x}(m+d, n+d)) \\
 F_{LCD_2}(m, n) &= \alpha \times \mathbf{x}(m, n) - \beta \times (\mathbf{x}(m, n-d) + \mathbf{x}(m, n+d)) \\
 F_{LCD_3}(m, n) &= \alpha \times \mathbf{x}(m, n) - \beta \times (\mathbf{x}(m-d, n+d) + \mathbf{x}(m+d, n-d)) \\
 F_{LCD_4}(m, n) &= \alpha \times \mathbf{x}(m, n) - \beta \times (\mathbf{x}(m-d, n) + \mathbf{x}(m+d, n))
 \end{aligned} \tag{3}$$

To further accentuate this difference, we define the Local Contrast Attention ( $LCA$ ) weight for the pixel at the coordinate  $(m, n)$  on the original image as follows:

$$W_{LCA}(m, n) = \text{Sigmod}(F_{LCD_1}(m, n) \times F_{LCD_2}(m, n) + F_{LCD_3}(m, n) \times F_{LCD_4}(m, n)) \tag{4}$$

The aforementioned procedure to acquire attention matrix  $\mathbf{W}_{LCA}$  can be formally expressed using tensor operations:

$$\mathbf{W}_{LCA} = F_{LCD_1} \odot F_{LCD_2} \oplus F_{LCD_3} \odot F_{LCD_4} \tag{5}$$

here  $\odot$  denotes the element-wise product,  $\oplus$  denotes the element-wise summation. If current pixel lies in the target area, the calculated  $LCD$  values should be larger, which means  $LCA$  value would approximate 1; when the pixel is located within the background area, the calculated  $LCD$  values should be smaller, which means  $LCA$  value would approximate 0.5. We use a simple case here to illustrate above computations, which is depicted in Fig. 4. In our case, we set  $\alpha$  as 1,  $\beta$  as 0.5 and  $d$  as 1.

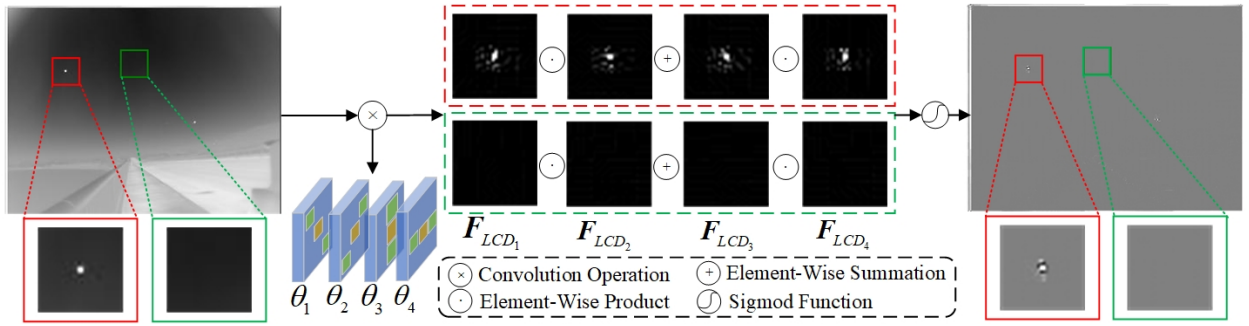


Fig. 4: Illustration of the computation process of our LCE module. In our case, we set  $\alpha$  as 1,  $\beta$  as 0.5 and  $d$  as 1.

The red rectangular box in the image contains a small target, while the green rectangular box only contains background pixels. Upon examination of the visualization results, it becomes evident that within the attention matrix  $W_{LCA}$ , the infrared small target stands out prominently in highlights, with the majority of remaining areas appearing predominantly gray. This indicates that irrelevant background information presenting in the original image has been effectively suppressed, highlighting the potential target areas. If we multiply  $W_{LCA}$  with the primary feature map  $F_0$ , the pixels located in target area would have minimal change in gray level while those located in background area would have decrease in gray level. So the calculated attention matrix  $W_{LCA}$  are element-wise multiplied with the primary feature map  $F_0$  to obtain the enhanced feature map  $F_0^{e1} \in \mathbb{R}^{C \times H \times W}$ , which could guide the constructed neural network model to pay more attention to potential infrared small targets:

$$F_0^{e1} = W_{LCA} \odot F_0 \quad (6)$$

After undergoing the processing of depthwise separable convolution and batch normalization, we obtain the resulting feature map  $F_0^{e2} \in \mathbb{R}^{C \times H \times W}$ , which mainly achieves the suppression of the background region. By element-wise adding  $F_0^{e2}$  to  $F_0$ , the useful contextual information of the primary feature map is preserved, completing background suppression while enhance the potential target region. Meanwhile, due to the introduction of residual structure, the proposed neural network model will be easier to optimize. It is followed by activation through the PReLU function to output the primary enhanced feature map  $F_0^e \in \mathbb{R}^{C \times H \times W}$ . The computational process can be represented as follows:

$$\begin{aligned} F_0^{e2} &= BN(DW(F_0^{e1})) \\ F_0^e &= PReLU(F_0 + F_0^{e2}) \end{aligned} \quad (7)$$

where  $DW$  denotes depthwise separable convolution and  $BN$  denotes batch normalization layer.

### 3.3. Channel Attention Enhancement module

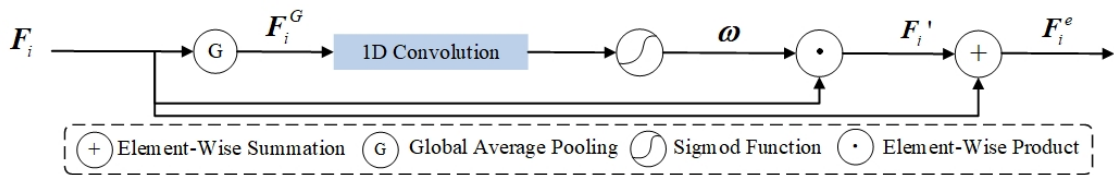


Fig. 5: Structure of CAE module.

With the progress of downsampling, the response information is distributed across the channels of output feature maps. To effectively utilize the information among different channels, fusing the information from each channel is a proven method. The CAE module is proposed to fuse information from different channels, and four CAE modules constitute the enhancing stage. By applying attention weighting to the multi-scale output feature map  $F_i (i = 1, 2, 3, 4)$  from four residual layers in the encoding stage, the weighted feature map  $F_i' (i = 1, 2, 3, 4)$  is obtained, which could reinforce the focus on potential infrared small target areas. By adding the original input feature map  $F_i$  to the weighted feature maps  $F_i'$  at the spatial level, the useful contextual information in the original input feature map is further fused

with the channel-weighting information, ultimately generating the enhanced feature map  $F_i^e$ . The structure of CAE module is illustrated in Fig. 5.

For the input feature map  $F_i \in \mathbf{R}^{C_i \times H_i \times W_i}$ , we initially apply global average pooling to obtain the feature representation  $F_i^G \in \mathbf{R}^{1 \times H_i \times W_i}$  ( $i = 1, 2, 3, 4$ ) based on global spatial information. Subsequently, inspired by (Rahman and Wang, 2016), we use a one-dimensional convolution with a kernel size of 3 to interact with the current channel and its two adjacent channels, which could achieve the fusion of channel information with a relatively small number of parameters. The Sigmoid activation function is then used to output the weight values  $\omega_j \in \omega$  ( $j = 1, 2, \dots, C$ ) for each channel. These weight values are multiplied point-wise with the input feature map to obtain the weighted feature map  $F_i' \in \mathbf{R}^{C_i \times H_i \times W_i}$ :

$$F_i' = F_i \odot \omega \quad (8)$$

We then add this to original input feature map  $F_i$ , ultimately yielding the enhanced feature map  $F_i^e \in \mathbf{R}^{C_i \times H_i \times W_i}$  ( $i = 1, 2, 3, 4$ ):

$$F_i^e = F_i' + F_i \quad (9)$$

By adding the channel-wise weighted result  $F_i'$  to the original input feature map  $F_i$ , the enhanced feature map could effectively retain the original contextual information while strengthening the semantic information at the locations of infrared small targets across different channel. This approach facilitates feature fusion and preservation of contextual information, aiding in the propagation of semantic information towards higher-resolution network layers during the decoding process, ultimately enabling precise pixel prediction. Furthermore, the integration of the weighted feature map with the original input feature map results in the adoption of a residual architecture within this module. This design facilitates the smooth backpropagation of gradients throughout the decoding and encoding stages, thereby enhancing the training efficiency of the LCAE-Net.

## 4. Experiments

### 4.1. Experiments setting

#### 4.1.1. Datasets

The experiments conducted in this paper utilize three publicly available datasets for single-frame infrared small target detection: NUAA-SIRST (Dai et al., 2021a), NUDT-SIRST (Li et al., 2022), and IRSTD-1K (Zhang et al., 2022b). These datasets comprise 427, 1327 and 1000 images respectively. Here, we follow the rule from Li et al. (2022) to partition the training and test sets of NUAA-SIRST and NUDT-SIRST, and from Zhang et al. (2022b) to split IRSTD-1K.

#### 4.1.2. Evaluation Metrics

To verify the effectiveness of our method, we use several standard metrics.

- (1) *IoU*: It is defined as the ratio of the number of pixels in the intersection area between the predicted mask and the label mask to the number of pixels in the union area. The calculation formula is as follows:

$$IoU = \frac{A_i}{A_u} = \frac{\sum_{i=1}^N TP_i}{\sum_{i=1}^N T_i + P_i - TP_i} \quad (10)$$

Here  $A_i$  and  $A_u$  denote the number of pixels in the intersection region and union region respectively,  $N$  denotes the number of samples tested,  $TP_i$  denotes the number of accurately predicted pixels in the  $i$ -th sample, while  $T_i$  and  $P_i$  represent the number of pixels in the Ground Truth and the method's prediction results for the sample to be tested respectively.

- (2) *P<sub>d</sub>*:  $P_d$  calculates the ratio of the number of correctly detected targets  $N_{pred}$  to the total number of targets  $N_{all}$  in the image. The calculation formula is as follows:

$$P_d = \frac{N_{pred}}{N_{all}} \quad (11)$$

Here, following (Li et al., 2022), we consider the target correctly predicted if the deviation of target centroid is less than 3.



**Table 1**

Comparisons with SOTA methods on three public datasets. The optimal value and the suboptimal value in each column are highlighted in **bold** and underline respectively.

Method	NUAA-SIRST			NUDT-SIRST			IRSTD-1K		
	$IoU/\%$	$P_d/\%$	$F_a/10^{-6}$	$IoU/\%$	$P_d/\%$	$F_a/10^{-6}$	$IoU/\%$	$P_d/\%$	$F_a/10^{-6}$
DNA-Net (Li et al., 2022)	74.092	<u>95.420</u>	37.779	91.959	98.412	9.077	<u>64.145</u>	89.562	<b>14.670</b>
ALCNet (Dai et al., 2021b)	68.275	91.985	32.195	64.667	97.989	38.124	<u>57.371</u>	91.246	51.755
ACM (Dai et al., 2021a)	69.729	90.840	31.229	66.576	96.402	19.464	56.915	91.582	82.709
UIU-Net (Wu et al., 2022)	<u>76.950</u>	93.130	<u>14.132</u>	87.231	97.883	<u>1.907</u>	61.884	93.939	48.225
RDIAN (Sun et al., 2023)	<u>71.558</u>	95.038	52.394	81.928	97.566	10.157	61.759	92.256	55.759
ISTDU-Net (Hou et al., 2022)	75.674	95.038	30.333	91.321	98.307	7.514	63.334	93.266	29.986
SCTransNet (Yuan et al., 2024)	75.024	<u>95.420</u>	39.157	<u>92.992</u>	<u>98.730</u>	3.102	63.997	<u>94.276</u>	<u>18.314</u>
LCAE-Net	<b>80.421</b>	<b>96.565</b>	<b>11.720</b>	<b>94.746</b>	<b>99.259</b>	<b>1.034</b>	<b>70.730</b>	<b>95.286</b>	19.017

- (3)  $F_a$ : It calculates the ratio of the number of incorrectly predicted pixels  $N_{false}$  to the total number of pixels  $P_{all}$  in the image. The calculation formula is as follows:

$$F_a = \frac{N_{false}}{P_{all}} \quad (12)$$

#### 4.1.3. Implementation details

The experiments were conducted under the Ubuntu 18.04 operating system. The workstation utilized were equipped with one Intel i9-9900K central processing unit and 64 GB of memory, one NVIDIA GeForce RTX 3090 with 24 GB of graphics memory. All code was implemented using the Pytorch framework. During the training process, the input images were standardized and then resized to 256×256 pixels through edge padding and random cropping, and data augmentation was performed using random flipping. The number of training epochs was set to 400, the batch size was 16, and the loss function we used was the Soft-IoU loss (Rahman and Wang, 2016). Parameters were updated using the Adam optimizer, with an initial learning rate of 0.0005, a momentum term of 0.9, and a polynomial decay learning rate scheduling strategy was adopted. The learning rate decay rate was set to 0.1, with adjustments made at epochs 200 and 300. In terms of hyperparameters,  $\alpha$  was set to 1,  $\beta$  was set to 0.5, and  $d$  was set to 3. The values of other parameters and the results are detailed in Section 4.4.

## 4.2. Results and analysis

To evaluate the proposed method more objectively and comprehensively, we compare our model to the state-of-the-art (SOTA) IRSTD methods, including: DNA-Net (Li et al., 2022), ALCNet (Dai et al., 2021b), ACM (Dai et al., 2021a), UIU-Net (Wu et al., 2022), RDIAN (Sun et al., 2023), ISTDU-Net (Hou et al., 2022) and SCTransNet (Yuan et al., 2024). Open-source implementations of these techniques can be found at github<sup>1</sup>. Comparative methods were trained in default hyperparameters from scratch using the same experimental settings. The performance of each method on the three public datasets is shown in Table 1, where the optimal value and the suboptimal value in each column are highlighted in **bold** and underline respectively.

We can see from the Table 1 that LCAE-Net outperforms the other SOTA methods and has achieved excellent test results on three benchmark datasets. Specifically, in terms of  $IoU$  metric, LCAE-Net has reached 80.421%, 94.746% and 70.730% respectively on the three datasets, outperforming the second-ranked method by 3.651%, 1.742% and 6.585%, demonstrating a significant advantage over the second-ranked method. In terms of  $P_d$ , LCAE-Net has achieved 96.565%, 99.259% and 95.286% on three datasets, surpassing the second-ranked method by 0.764%, 1.742%, and 1.01% respectively. As for  $F_a$ , LCAE-Net excels on the NUAA-SIRST and NUDT-SIRST datasets with  $11.720 \times 10^{-6}$  and  $1.034 \times 10^{-6}$  separately, but is marginally less effective than DNA-Net and SCTransNet on the IRSTD-1K dataset. The dense nested interactive connection of DNA-Net and the Spatial-channel Cross Transformer Block (SCTB) of SCTransNet facilitate multiple enhancements of semantic information at the expense of computational efficiency, which make them have certain advantages when confronted with datasets like IRSTD-1K, which including varying-shape targets and background with clutters and noises. Overall, our method exhibits favorable results across the three datasets. Additionally, Table 1 indicates that DNA-Net, UIU-Net, and SCTransNet exhibit strong competitiveness with

<sup>1</sup><https://github.com/XinyiYing/BasicIRSTD> and <https://github.com/xdFaiAll>

**Table 2**

 Comparison of model complexity and detection speed, where the optimal value in each column is highlighted in **bold**.

Method	Params (M)	FLOPs (G)	Speed (fps)
DNA-Net (Li et al., 2022)	4.697	14.261	40.49
UIU-Net (Wu et al., 2022)	50.540	54.426	54.17
SCTransNet (Yuan et al., 2024)	11.191	10.119	33.62
LCAE-Net	<b>1.945</b>	<b>4.862</b>	<b>70.23</b>

our method in these three metrics. Table 2 presents a comparison of these methods in terms of model parameter size, FLOPs and detection speed, calculated using images with a resolution of  $256 \times 256$ , where the optimal value in each column is highlighted in **bold**.

Considering the complexity and performance of each method, although our LCAE-Net has a small gap in  $F_a$  on the IRSTD-1K dataset, its parameters, FLOPs and detection speed are 1.945M, 4.862G and 70.23fps respectively, representing a substantial computation cost reduction and high real-time performance compared to competitive methods. This indicates that our LCAE-Net effectively balances the demands for computational complexity and detection performance, making it more suitable for deployment on edge infrared detection devices with limited resources. To visually evaluate the differences in detection effects among these methods, we select two typical infrared scenarios from each of the three public datasets and compares the detection results of six detection methods. The visualizations and corresponding saliency maps are shown in Fig. 6 and Fig. 7, while in Fig. 6, the red, green, and yellow circles represent correctly detected targets, missed detection, and false alarms respectively.

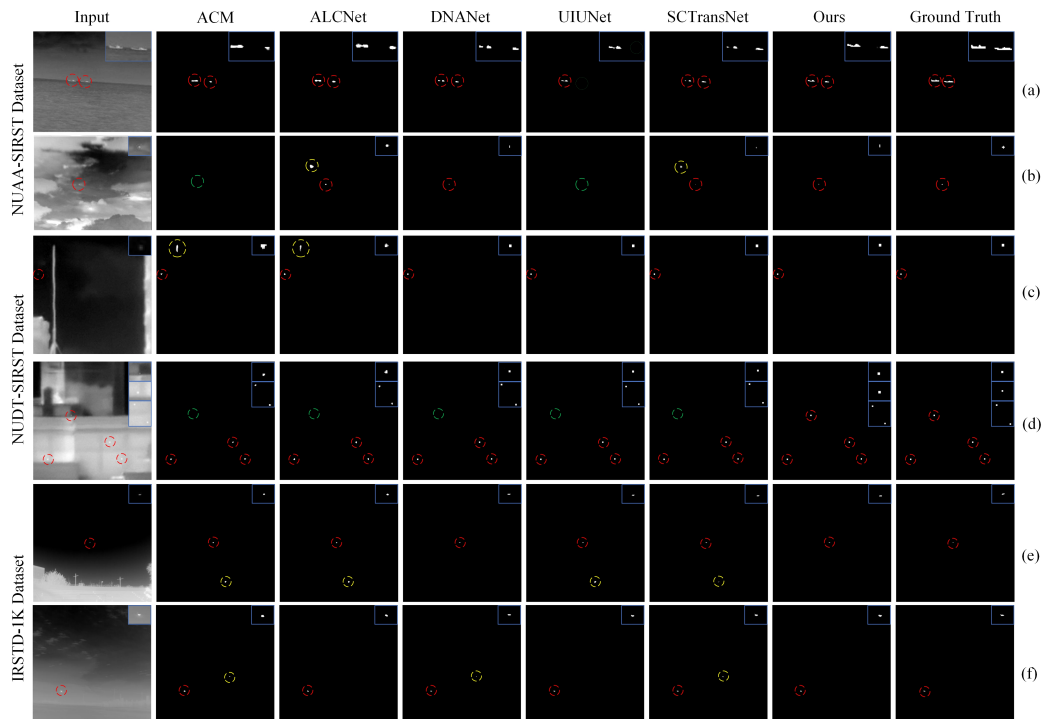


**Fig. 6:** Visual results obtained by different IRSTD methods. The red, green, and yellow circles represent correctly detected targets, missed detection, and false alarms respectively.

From two figures we can observe that our method has achieved satisfactory detection results across all six scenarios. In scenario (a), the original image depicts two closely adjacent ships on the sea. Our LCAE-Net accurately detects the shape of two ships. In contrast, except for ACM and ALCNet, the other methods detect the left target as two separate entities, demonstrating that the our method is more suitable for detecting strip-like targets. It is worth noting that comparing to ALCNet which uses similar multiscale local contrast enhancing method, our detection result is more precise, which indicates a single-scale operator with appropriate prior knowledge is sufficient to produce satisfactory results. Scenarios (b) and (f) are infrared small targets in the sky. In scenario (b), ACM and UIUNet miss targets, while

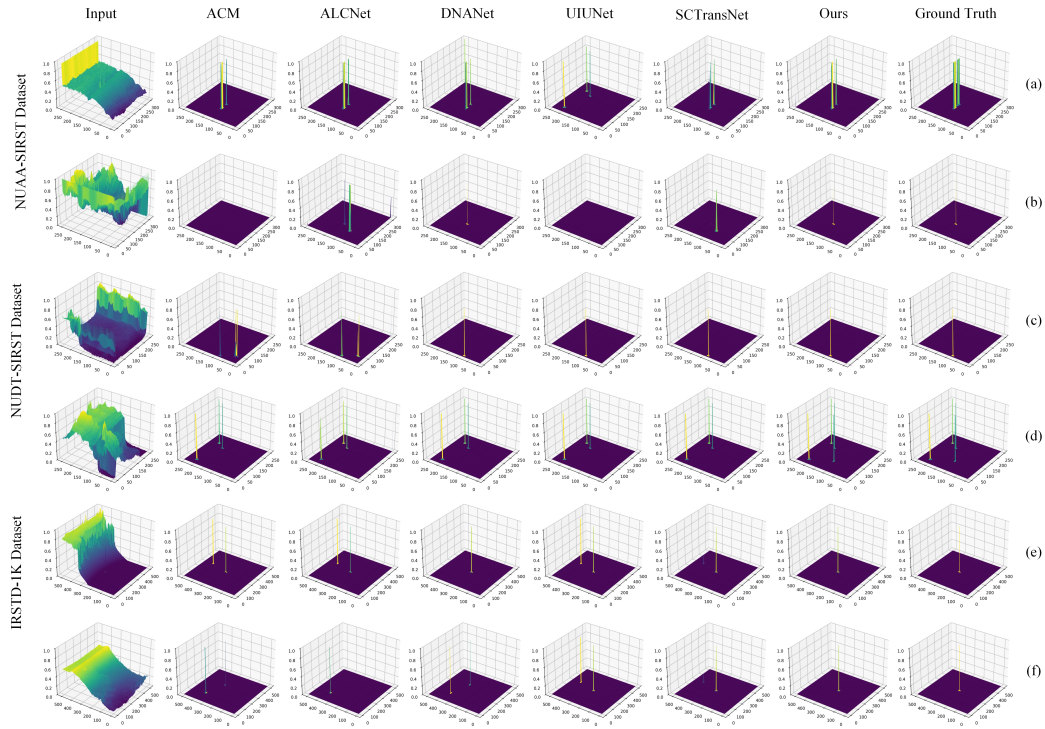


Fig. 7: 3D visualization of salient maps of different methods on six test images.

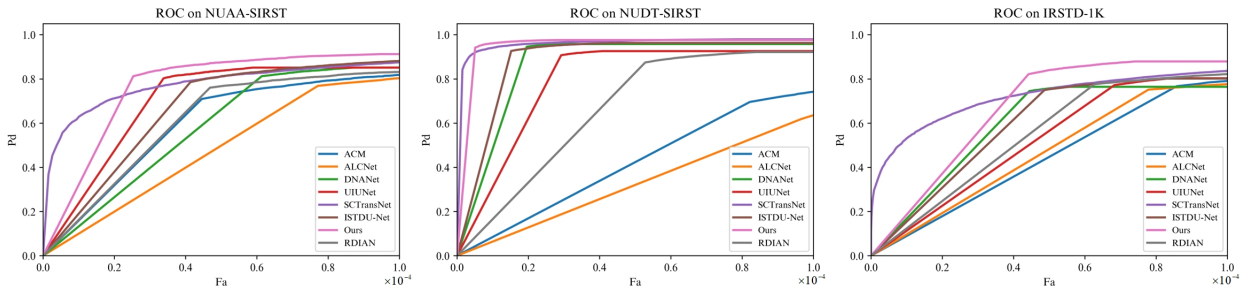


Fig. 8: ROC curves of different methods on three datasets.

ALCNet and SCTransNet have false alarms. In scenario (f), ACM, DNANet, and SCTransNet all have false alarms. Our LCAE-Net achieves better detection results in both scenarios, indicating that the proposed LCE module could guide the network model to pay more attention on real positions of small targets. In scenario (c), the tail flame of the rocket is misdected by ACM and ALCNet, and in scenario (e), the street lamp is misdected by ACM, ALCNet, UIUNet, and SCTransNet. Our method exhibits good detection performance in these two scenarios, highlighting its effectiveness in suppressing irrelevant background interference. In scenario (d), all other methods except the one we proposed miss targets, indicating that even dim targets can be effectively detected with the assistance of appropriate prior knowledge.

Fig. 8 shows the Receiver Operating Characteristic (ROC) curves of different methods across three datasets. A ROC curve reflects the detection capability of one method. From Fig. 8, it could be seen that our LCAE-Net achieve a high detection probability at a very low false alarm rate, proving the superiority of it.

### 4.3. Ablation study

In order to demonstrate the effectiveness of our major modules, we conducted ablation experiments on three benchmark datasets using the same implementation details in Section 4.1.3. The experimental results are shown in Table 3, and the optimal value in each column is highlighted in **bold**.

**Table 3**

 Results of ablation experiments. The optimal value in each column is highlighted in **bold**.

CAE	LCE	NUAA-SIRST			NUDT-SIRST			IRSTD-1K		
		$IoU/\%$	$P_d/\%$	$F_a/10^{-6}$	$IoU/\%$	$P_d/\%$	$F_a/10^{-6}$	$IoU/\%$	$P_d/\%$	$F_a/10^{-6}$
		77.733	94.656	22.336	92.887	98.836	2.918	67.250	94.613	54.620
✓		78.465	96.183	29.782	93.122	99.048	2.827	68.679	94.613	30.986
	✓	78.847	<b>96.565</b>	21.233	93.729	99.048	2.735	68.342	94.949	35.243
✓	✓	<b>80.421</b>	<b>96.565</b>	<b>11.720</b>	<b>94.746</b>	<b>99.259</b>	<b>1.034</b>	<b>70.730</b>	<b>95.286</b>	<b>19.017</b>

**Table 4**

 Analysis of the hyperparameters. The optimal value and the suboptimal value in each column are highlighted in **bold** and underline respectively.

$d$	$\alpha$	$\beta$	NUAA-SIRST			NUDT-SIRST			IRSTD-1K		
			$IoU/\%$	$P_d/\%$	$F_a/10^{-6}$	$IoU/\%$	$P_d/\%$	$F_a/10^{-6}$	$IoU/\%$	$P_d/\%$	$F_a/10^{-6}$
1	1	0.5	<b>80.421</b>	<b>96.565</b>	<b>11.720</b>	<b>94.746</b>	<b>99.259</b>	<b>1.034</b>	<b>70.730</b>	<b>95.286</b>	<b>19.017</b>
	1	1	78.447	95.802	26.059	<u>93.863</u>	<u>99.153</u>	2.964	66.818	94.613	32.207
	1.5	0.5	78.248	<u>96.183</u>	25.507	93.165	98.519	1.999	67.787	<u>94.949</u>	42.322
	1.5	1	77.263	95.038	24.335	93.172	<u>99.153</u>	4.803	67.195	92.929	41.848
	2	0.5	78.113	93.130	28.748	93.525	98.836	3.309	66.036	94.276	48.737
	2	1	77.044	<b>96.565</b>	23.232	93.078	98.942	3.815	65.950	93.939	51.166
2	1	0.5	<u>79.551</u>	<b>96.565</b>	12.409	93.019	98.730	1.655	68.538	93.939	38.887
	1	1	<u>77.541</u>	95.038	23.784	93.221	<b>99.259</b>	3.746	66.196	<u>94.949</u>	42.170
	1.5	0.5	77.510	94.275	36.882	93.195	98.624	1.861	66.083	<u>93.266</u>	<u>29.701</u>
	1.5	1	77.112	95.420	38.123	92.339	98.307	4.665	67.697	94.613	34.370
	2	0.5	79.535	<u>96.183</u>	19.785	93.722	98.942	2.895	64.316	93.603	41.639
	2	1	77.735	<u>95.802</u>	35.779	92.688	98.834	3.907	66.144	94.276	43.632
3	1	0.5	79.347	<b>96.565</b>	29.782	93.172	98.941	2.528	<u>68.706</u>	93.939	36.439
	1	1	77.059	93.893	37.434	92.941	98.730	2.045	68.395	94.276	31.239
	1.5	0.5	78.492	94.656	28.748	93.016	98.519	2.436	68.581	<u>94.949</u>	36.610
	1.5	1	78.410	95.802	32.263	93.841	98.836	1.976	68.123	94.613	35.907
	2	0.5	79.025	<u>96.183</u>	41.984	92.909	98.413	3.700	67.222	93.602	34.731
	2	1	77.679	<u>95.038</u>	34.814	93.172	98.624	2.666	66.253	<b>95.286</b>	45.890
4	1	0.5	79.053	<u>96.183</u>	40.743	92.733	98.413	<u>1.310</u>	67.288	<b>95.286</b>	46.421
	1	1	78.903	95.802	30.678	92.291	98.836	4.895	68.849	<u>94.949</u>	34.086
	1.5	0.5	76.444	95.038	19.579	93.730	<u>99.153</u>	1.563	67.118	95.623	32.017
	1.5	1	78.023	<b>96.565</b>	22.060	92.860	98.942	5.079	68.234	94.276	39.779
	2	0.5	78.121	94.656	29.161	93.016	98.624	1.792	67.946	94.613	35.870
	2	1	78.872	95.420	28.196	92.859	98.519	3.723	68.121	94.613	43.423

The first line of results in Table 3 represent the network after replacing CAE module with element-wise summation and removing LCE module. Comparing the first and second lines, it becomes apparent that integrating the proposed CAE module enhances the network's performance, resulting in improvements of 0.732%, 0.235%, and 1.429% in  $IoU$  across the three datasets. Additionally,  $P_d$  metric increases by 1.527% and 0.212% on the NUAA-SIRST and NUDT-SIRST datasets separately, while  $F_a$  metric decreases by  $0.091 \times 10^{-6}$  and  $23.634 \times 10^{-6}$  on the NUDT-SIRST and IRSTD-1K datasets, validating the efficacy of the proposed CAE module. Furthermore, a comparison between the first and third line highlights improvements in all evaluation metrics on the three datasets, with the  $P_d$  metric on the NUAA-SIRST dataset achieving the optimal value in its column, thereby confirming the effectiveness of the developed LCE module. Lastly, comparing to integrate only one module, data from the first to the fourth lines presents the remarkable impact of utilizing the CAE and LCE modules simultaneously. This combination leads to optimal results across all metrics, emphasizing the substantial boost in network performance delivered by our proposed modules.

#### 4.4. Hyperparameter Analysis

The LCE module incorporates two hyperparameters  $\alpha$  and  $\beta$ , with the objective of emphasizing the pixels at the potential infrared small target in the image. Inspired by the design of fixed convolution operators utilized in methods such as RDIAN (Sun et al., 2023) and MPCM (Wei et al., 2016), it is reasonable to assume that the values of  $\alpha$

**Table 5**

Analysis of the refined hyperparameters. The optimal value and the worst value in each column are highlighted in **bold** and underline respectively.

$\alpha$	$\beta$	NUAA-SIRST			NUDT-SIRST			IRSTD-1K		
		$IoU/\%$	$P_d/\%$	$F_a/10^{-6}$	$IoU/\%$	$P_d/\%$	$F_a/10^{-6}$	$IoU/\%$	$P_d/\%$	$F_a/10^{-6}$
0.5	0.25	78.402	<b>96.565</b>	22.060	93.791	99.153	2.367	68.595	94.613	31.542
0.5	0.5	78.057	95.420	18.269	93.698	98.942	2.068	67.522	94.949	33.023
0.5	0.75	<u>76.131</u>	94.656	32.884	93.185	<u>98.413</u>	4.964	67.211	94.613	38.697
0.5	1	<u>77.867</u>	94.274	30.057	93.095	<u>98.730</u>	2.620	65.983	93.266	34.199
1	0.25	77.774	93.893	28.748	93.023	98.836	3.654	67.760	93.603	30.252
1	0.5	<b>80.421</b>	<b>96.565</b>	<b>11.720</b>	<b>94.746</b>	<b>99.259</b>	<b>1.034</b>	<b>70.730</b>	<b>95.286</b>	<b>19.017</b>
1	0.75	78.492	95.420	28.127	93.571	98.730	1.792	65.445	<b>95.286</b>	40.178
1	1	78.447	95.802	26.059	93.321	98.836	3.516	66.818	94.613	32.207
1.5	0.25	78.089	94.656	31.574	93.277	98.624	1.746	66.507	94.613	32.700
1.5	0.5	78.248	96.183	25.507	93.165	98.519	1.999	67.787	94.949	42.322
1.5	0.75	77.702	95.802	25.163	93.152	99.153	<u>5.377</u>	67.311	94.613	33.592
1.5	1	77.263	95.038	24.335	93.172	99.153	4.803	67.195	<u>92.929</u>	41.848
2	0.25	76.824	94.275	<u>33.849</u>	<u>92.949</u>	98.730	3.102	66.975	93.603	37.046
2	0.5	78.113	<u>93.130</u>	28.748	93.525	98.836	3.309	66.036	94.276	48.737
2	0.75	78.540	<b>96.565</b>	21.647	93.824	98.519	2.964	<u>64.161</u>	94.613	37.331
2	1	77.044	<b>96.565</b>	23.232	93.078	98.942	3.815	<u>65.950</u>	93.939	51.166
<i>distance</i>		4.290	3.435	22.129	1.797	0.846	4.343	6.569	2.357	32.149

and  $\beta$  should not exhibit significant disparities. Therefore, the value range for hyperparameter  $\alpha$  is designated at  $\alpha \in \{1, 1.5, 2\}$ , while for  $\beta$ , the value range is set as  $\beta \in \{0.5, 1\}$ . Given that infrared small targets generally do not exceed in size  $9 \times 9$  within the image, and considering that the convolution kernel size should be an odd number, the value range for  $d$  is set as  $d \in \{1, 2, 3, 4\}$ . The experimental results under different hyperparameter settings are displayed in Table 4, where the optimal value and the suboptimal value in each column are highlighted in **bold** and underline respectively.

We can see from the Table 4 that when  $d$  is fixed, LCAE-Net performs well on the three datasets when  $\alpha$  and  $\beta$  are set to 1 and 0.5, and the global optimal value is acquired when  $d$  is set to 1. We conclude that for  $d$ , due to the generally small size of infrared small targets, when the value is too large, the convolution operator covers an excessive amount of non-target area. This leads to interactions between the center pixel and distant, irrelevant pixels, ultimately making it challenging to enhance performance. To further explore the impact of  $\alpha$  and  $\beta$ , we fixed  $d$  at 1 and refined the value range of  $\alpha$  and  $\beta$ . Here the value range for hyperparameter  $\alpha$  is designated at  $\alpha \in \{0.5, 1, 1.5, 2\}$ , while for  $\beta$ , the value range is set as  $\beta \in \{0.25, 0.5, 0.75, 1\}$ . The experimental results on the three datasets are shown in Table 5. The optimal value and the worst value in each column are highlighted in **bold** and underline respectively, and the last line shows the distance between the two values.

As evident from the data presented in the Table 5, LCAE-Net exhibits the strongest robustness on  $P_d$  metric, with distances across the three datasets being 3.435%, 0.846%, and 2.357% respectively, indicating its effectiveness in detecting infrared small targets in images. In terms of  $IoU$  and  $F_a$  metrics, the method performs well on the NUAA-SIRST and NUDT-SIRST datasets, with extreme differences of 4.290%,  $22.129 \times 10^{-6}$ , and 1.797%,  $4.343 \times 10^{-6}$  respectively. However, on the IRSTD-1K dataset, the robustness is slightly weaker, with extreme differences of 6.569% and  $32.149 \times 10^{-6}$  for the two metrics. This is because the IRSTD-1K dataset contains a diverse range of infrared small targets across various scenes such as oceans, rivers, fields, mountains, cities, and clouds. The relatively severe clutter and noise in these scenes render this dataset highly sensitive to hyperparameter values. This could explain the slightly weaker performance of the proposed method on the IRSTD-1K dataset. Additionally, we can see from the table that when the difference between values of  $\alpha$  and  $\beta$  is too large (see  $\alpha=2$  and  $\beta=0.25$ ), LCAE-Net may perform weakly. This may be due to the fact that when the difference is too large, the calculated  $LCD$  value consistently exhibits a large negative absolute value, thus leading to the large  $LCA$  value and decreasing the discrimination. In this situation, whether the convolution operator passes through a target pixel or a background pixel, it will smooth the entire image and reduce the disparity in grayscale values between pixels on the original image, making it difficult for the detection network to

effectively identify the target. When we choose hyperparameters in practice, it is advisable for us not allow for a large gap between these two values.

## 5. Conclusion

This paper proposes an infrared small target detection method called LCAE-Net that seamlessly integrates model-driven and data-driven approaches, incorporating prior knowledge into the neural network's learning and distinguishing process. In this model, we design the LCE module to guide the neural network's focus towards the spatial location of infrared small targets, and propose the CAE module to efficiently fuse and enhance information across different channels. Experimental results indicate that the proposed method has achieved favorable outcomes on three publicly available infrared small target datasets. Furthermore, its parameter size and FLOPs are relatively small, making it suitable for deployment on edge devices with limited computational resources.

The LCAE-Net proposed in our paper has achieved a commendable balance between detection performance and computational cost. There still exists improving space in false alarm rate. In future, we will continuously optimizing the model to decrease its false alarm rate, and practical deploy it on low-resource devices.

## References

- Bi, Y., Chen, J., Sun, H., Bai, X., 2019. Fast detection of distant, infrared targets in a single image using multiorder directional derivatives. *IEEE Transactions on Aerospace and Electronic Systems* 56, 2422–2436. doi:10.1109/TAES.2019.2946678.
- Chapple, P.B., Bertilone, D.C., Caprari, R.S., Angeli, S., Newsam, G.N., 1999. Target detection in infrared and sar terrain images using a non-gaussian stochastic model, in: *Targets and backgrounds: characterization and representation V*, SPIE. pp. 122–132.
- Chen, C.P., Li, H., Wei, Y., Xia, T., Tang, Y.Y., 2013. A local contrast method for small infrared target detection. *IEEE transactions on geoscience and remote sensing* 52, 574–581. doi:10.1109/TGRS.2013.2242477.
- Chen, Y., Li, L., Liu, X., Su, X., 2022. A multi-task framework for infrared small target detection and segmentation. *IEEE Transactions on Geoscience and Remote Sensing* 60, 1–9. doi:10.1109/TGRS.2022.3195740.
- Cui, Y., Lei, T., Chen, G., Zhang, Y., Peng, L., Hao, X., Zhang, G., 2024. Hollow side window filter with saliency prior for infrared small target detection. *IEEE Geoscience and Remote Sensing Letters* 21, 1–5. doi:10.1109/LGRS.2023.3342981.
- Dai, Y., Wu, Y., 2017. Reweighted infrared patch-tensor model with both nonlocal and local priors for single-frame small target detection. *IEEE journal of selected topics in applied earth observations and remote sensing* 10, 3752–3767. doi:10.1109/JSTARS.2017.2700023.
- Dai, Y., Wu, Y., Song, Y., 2016. Infrared small target and background separation via column-wise weighted robust principal component analysis. *Infrared Physics & Technology* 77, 421–430. doi:10.1016/j.infrared.2016.06.021.
- Dai, Y., Wu, Y., Zhou, F., Barnard, K., 2021a. Asymmetric contextual modulation for infrared small target detection, in: *Proceedings of the IEEE/CVF winter conference on applications of computer vision*, pp. 950–959. doi:10.1109/WACV48630.2021.00099.
- Dai, Y., Wu, Y., Zhou, F., Barnard, K., 2021b. Attentional local contrast networks for infrared small target detection. *IEEE transactions on geoscience and remote sensing* 59, 9813–9824. doi:10.1109/TGRS.2020.3044958.
- Deshpande, S.D., Er, M.H., Venkateswarlu, R., Chan, P., 1999. Max-mean and max-median filters for detection of small targets, in: *Signal and Data Processing of Small Targets 1999*, SPIE. pp. 74–83.
- Gao, C., Meng, D., Yang, Y., Wang, Y., Zhou, X., Hauptmann, A.G., 2013. Infrared patch-image model for small target detection in a single image. *IEEE transactions on image processing* 22, 4996–5009. doi:10.1109/TIP.2013.2281420.
- Girshick, R., Donahue, J., Darrell, T., Malik, J., 2014. Rich feature hierarchies for accurate object detection and semantic segmentation, in: *Proceedings of the IEEE/CVF conference on computer vision and pattern recognition*, pp. 580–587.
- He, S., Pan, S., An, B., 2024. Infrared small target detection based on variance difference weighted three-layer local contrast measure. *Infrared Physics & Technology* 139, 105315. doi:10.1016/j.infrared.2024.105315.
- Hou, Q., Zhang, L., Tan, F., Xi, Y., Zheng, H., Li, N., 2022. Istdu-net: Infrared small-target detection u-net. *IEEE Geoscience and Remote Sensing Letters* 19, 1–5. doi:10.1109/LGRS.2022.3141584.
- Hu, J., Shen, L., Sun, G., 2020. Squeeze-and-excitation networks. *IEEE Transactions on Pattern Analysis and Machine Intelligence* 42, 2011–2023. doi:10.1109/TPAMI.2019.2913372.
- Hu, L., Yang, D., Zhao, D., Zhang, J., 2024. Infrared small target detection method based on improved non-convex estimation and asymmetric spatial-temporal regularization. *Journal of National University of Defense Technology* 46, 180–194.
- Huang, S., Liu, Y., He, Y., Zhang, T., Peng, Z., 2019. Structure-adaptive clutter suppression for infrared small target detection: Chain-growth filtering. *Remote Sensing* 12, 47. doi:10.1109/TAES.2019.2946678.
- Jia, G., Cheng, Y., Chen, T., 2024. Irgraphseg: infrared small target detection based on hierarchical gnn. *IEEE Geoscience and Remote Sensing Letters* 21, 1–5. doi:10.1109/LGRS.2024.3374431.
- Kou, R., Wang, C., Peng, Z., Zhao, Z., Chen, Y., Han, J., Huang, F., Yu, Y., Fu, Q., 2023. Infrared small target segmentation networks: A survey. *Pattern Recognition* 143, 109788. doi:10.1016/j.patcog.2023.109788.
- Li, B., Xiao, C., Wang, L., Wang, Y., Lin, Z., Li, M., An, W., Guo, Y., 2022. Dense nested attention network for infrared small target detection. *IEEE Transactions on Image Processing* 32, 1745–1758. doi:10.1109/TIP.2022.3199107.
- Li, X., Wang, W., Hu, X., Yang, J., 2019. Selective kernel networks, in: *Proceedings of the IEEE/CVF conference on computer vision and pattern recognition*, pp. 510–519. doi:10.1109/CVPR.2019.00060.

- Liu, F., Gao, C., Chen, F., Meng, D., Zuo, W., Gao, X., 2023a. Infrared small and dim target detection with transformer under complex backgrounds. *IEEE Transactions on Image Processing* 32, 5921–5932. doi:10.1109/TIP.2023.3326396.
- Liu, Q., Liu, R., Zheng, B., Wang, H., Fu, Y., 2024. Infrared small target detection with scale and location sensitivity, in: *Proceedings of the IEEE/CVF Conference on Computer Vision and Pattern Recognition*, pp. 17490–17499.
- Liu, W., Anguelov, D., Erhan, D., Szegedy, C., Reed, S., Fu, C.Y., Berg, A.C., 2016. Ssd: Single shot multibox detector, in: *European conference on computer vision*, Springer. pp. 21–37.
- Liu, W., Lu, H., Fu, H., Cao, Z., 2023b. Learning to upsample by learning to sample, in: *Proceedings of the IEEE/CVF International Conference on Computer Vision*, pp. 6004–6014. doi:10.1109/ICCV51070.2023.00554.
- Liu, Y., Peng, Z., 2022. Infrared small target detection based on resampling-guided image model. *IEEE Geoscience and Remote Sensing Letters* 19, 1–5. doi:10.1109/LGRS.2021.3087799.
- Luo, H., Wang, F., Chen, Z., Yu, L., 2010. Infrared target detecting based on symmetrical displaced frame difference and optical flow estimation. *Acta Optica Sinica* 30, 1715–1720.
- M, C., 2011. Visual attention: the past 25 years. *Vision Research: An International Journal in Visual Science* 51, 1484–1525. doi:10.1016/j.visres.2011.04.012.
- Nian, B., Jiang, B., Shi, H., Zhang, Y., 2023. Local contrast attention guide network for detecting infrared small targets. *IEEE Transactions on Geoscience and Remote Sensing* 61, 1. doi:10.1109/TGRS.2023.3266447.
- Rahman, M.A., Wang, Y., 2016. Optimizing intersection-over-union in deep neural networks for image segmentation, in: *International symposium on visual computing*, Springer. pp. 234–244.
- Redmon, J., Divvala, S., Girshick, R., Farhadi, A., 2016. You only look once: Unified, real-time object detection, in: *Proceedings of the IEEE/CVF conference on computer vision and pattern recognition*.
- Shi, Y., Lin, Y., Wei, P., Xian, X., Chen, T., Lin, L., 2024. Diff-mosaic: augmenting realistic representations in infrared small target detection via diffusion prior. *IEEE Transactions on Geoscience and Remote Sensing* 61, 1–11. doi:10.1109/TGRS.2024.3408045.
- Sun, H., Bai, J., Yang, F., Bai, X., 2023. Receptive-field and direction induced attention network for infrared dim small target detection with a large-scale dataset irdst. *IEEE Transactions on Geoscience and Remote Sensing* 61, 1–13. doi:10.1109/TGRS.2023.3235150.
- Tianxiang, C., Zhentao, T., Tao, G., Qi, C., Yue, W., Bin, L., Jieping, Y., Nenghai, Y., 2024. Mim-istd: Mamba-in-mamba for efficient infrared small target detection. *arXiv preprint arXiv:2403.02148*.
- Wang, B., Song, Y., Dong, X., 2024. Indistinguishable points attention-aware network for infrared small object detection. *Chinese Optics* 17, 538–547.
- Wang, G., Tao, B., Kong, X., Peng, Z., 2021. Infrared small target detection using nonoverlapping patch spatial-temporal tensor factorization with capped nuclear norm regularization. *IEEE Transactions on Geoscience and Remote Sensing* 60, 1–17. doi:10.1109/TGRS.2021.3126608.
- Wang, H., Zhou, L., Wang, L., 2019. Miss detection vs. false alarm: Adversarial learning for small object segmentation in infrared images, in: *Proceedings of the IEEE/CVF International Conference on Computer Vision*, pp. 8509–8518. doi:10.1109/ICCV.2019.00860.
- Wang, K., Du, S., Liu, C., Cao, Z., 2022. Interior attention-aware network for infrared small target detection. *IEEE Transactions on Geoscience and Remote Sensing* 60, 1–13. doi:10.1109/TGRS.2022.3163410.
- Wei, Y., You, X., Li, H., 2016. Multiscale patch-based contrast measure for small infrared target detection. *Pattern Recognition* 58, 216–226. doi:10.1016/j.patcog.2016.04.002.
- Wu, A., Fan, X., Min, L., Qin, W., Yu, L., 2024. Dim and small target detection based on local feature prior and tensor train nuclear norm. *IEEE Photonics Journal* 16, doi:10.1109/JPHOT.2024.3351189.
- Wu, T., Li, B., Luo, Y., Wang, Y., Xiao, C., Liu, T., Yang, J., An, W., Guo, Y., 2023. Mtu-net: multilevel transunet for space-based infrared tiny ship detection. *IEEE Transactions on Geoscience and Remote Sensing* 61, 1–15. doi:10.1109/TGRS.2023.3235002.
- Wu, X., Hong, D., Chanussot, J., 2022. Uiu-net: U-net in u-net for infrared small object detection. *IEEE Transactions on Image Processing* 32, 364–376. doi:10.1109/TIP.2022.3228497.
- Xia, C., Chen, S., Huang, R., Hu, J., Chen, Z., 2024. Separable spatial-temporal patch-tensor pair completion for infrared small target detection. *IEEE Transactions on Geoscience and Remote Sensing* 62. doi:10.1109/TGRS.2024.3358831.
- Xia, C., Li, X., Zhao, L., Shu, R., 2019. Infrared small target detection based on multiscale local contrast measure using local energy factor. *IEEE Geoscience and Remote Sensing Letters* 17, 157–161. doi:10.1109/LGRS.2019.2914432.
- Yang, H., Mu, T., Dong, Z., Zhang, Z., Wang, B., Ke, W., Yang, Q., He, Z., 2024. Pbt: Progressive background-aware transformer for infrared small target detection. *IEEE Transactions on Geoscience and Remote Sensing* doi:10.1109/TGRS.2024.3415080.
- Yu, C., Liu, Y., Wu, S., Hu, Z., Xia, X., Lan, D., Liu, X., 2022. Infrared small target detection based on multiscale local contrast learning networks. *Infrared Physics & Technology* 123, 104107. doi:10.1016/j.infrared.2022.104107.
- Yu, F., Koltun, V., 2015. Multi-scale context aggregation by dilated convolutions. *arXiv preprint arXiv:1511.07122*.
- Yuan, S., Qin, H., Yan, X., Akhtar, N., Mian, A., 2024. Sctransnet: Spatial-channel cross transformer network for infrared small target detection. *IEEE Transactions on Geoscience and Remote Sensing* 62, 1–15. doi:10.1109/TGRS.2024.3383649.
- Zeng, M., Li, J., Peng, Z., 2006. The design of top-hat morphological filter and application to infrared target detection. *Infrared physics & technology* 48, 67–76. doi:10.1016/j.infrared.2005.04.006.
- Zhang, H., Wu, C., Zhang, Z., Zhu, Y., Lin, H., Zhang, Z., Sun, Y., He, T., Mueller, J., Manmatha, R., et al., 2022a. Resnest: split-attention networks, in: *Proceedings of the IEEE/CVF conference on computer vision and pattern recognition*, pp. 2736–2746. doi:10.1109/CVPRW56347.2022.00309.
- Zhang, L., Yang, H., Zheng, Q., Zhang, Y., Zhang, D., 2024. Infrared small target detection based on density peak search and local features. *IET Signal Processing* 2024, 6814362. doi:10.1016/j.infrared.2024.105315.
- Zhang, M., Zhang, R., Yang, Y., Bai, H., Zhang, J., Guo, J., 2022b. Isnet: shape matters for infrared small target detection, in: *Proceedings of the IEEE/CVF Conference on Computer Vision and Pattern Recognition*, pp. 877–886. doi:10.1109/CVPR52688.2022.00095.

- Zhang, T., Gao, Z., Liu, Z., Hussain, S.F., Waqas, M., Halim, Z., Li, Y., 2023. Infrared ship target segmentation based on adversarial domain adaptation. *Knowledge-Based Systems* 265, 110344. doi:10.1016/j.knsys.2023.110344.
- Zhao, J., Shi, Z., Yu, C., Liu, Y., 2024. Multi-scale direction-aware network for infrared small target detection. arXiv preprint arXiv:2406.02037 .
- Zhao, M., Li, L., Li, W., Tao, R., Li, L., Zhang, W., 2020. Infrared small-target detection based on multiple morphological profiles. *IEEE Transactions on Geoscience and Remote Sensing* 59, 6077–6091. doi:10.1109/TGRS.2020.3022863.
- Zhao, M., Li, W., Li, L., Hu, J., Ma, P., Tao, R., 2022. Single-frame infrared small-target detection: A survey. *IEEE Geoscience and Remote Sensing Magazine* 10, 87–119. doi:10.1109/MGRS.2022.3145502.